3D simulation of adiabatic shear bands in high speed machining

Fabien Delalondre, Simon Guerdoux, Lionel Fourment

3D Simulation of Adiabatic Shear Bands in High Speed Machining

Fabien Delalondre, Simon Guerdoux, Lionel Fourment*

CEMEF, Centre For Material Forming, Ecole des Mines de Paris,
1 Rue Claude Daunesse 06904 Sophia Antipolis, France
* Corresponding author: lionel.fourment@ensmp.fr

Abstract. A finite element model of three-dimensional high speed machining is developed. In order to catch Adiabatic Shear Band (ASB), which is about few microns wide, the simulation uses mesh adaptation triggered by an isotropic error estimator. An enhanced version of the Zienkiewicz and Booromand REP in Patches technique is used. As ASB is a much localized phenomenon, the adaptive procedure provides highly refined meshes with strong gradients of the element size, which makes it quite difficult to produce satisfactory 3D meshes. Furthermore, high speed machining leads to very important values of strain rate, deformation and possibly to extreme mesh distortion. So, an Arbitrary Lagrangian Eulerian (ALE) method is employed. With the utilized splitting method and linear finite element interpolation, the transport of nodal variables is based on the gradient calculated in the upwind element. For variables stored at the integration points, a remapping procedure using patch recovery techniques is preferred. Finally, because of the very strong thermo-mechanical coupling taking place in ASB, several thermo-mechanical coupling schemes are studied. Explicit and fully implicit schemes are compared, showing that the second one offers a stabilizing effect and a better accuracy. All of these ingredients provide a fully automatic and process independent procedure which allows detecting and following the formation of Adiabatic Shear Band in High Speed Machining. The creation of 3D segmented chip is observed and compared to 2D reference results obtained by Baker in [1]. The influence of numerical coefficients like the mesh size is investigated. Other application to actual 3D high speed machining such as blanking is also presented.

Keywords: Adiabatic Shear Band, High Speed Machining, Segmented Chip, Adaptive Remeshing, Error Estimation, 3D Meshing, ALE Formulation, Implicit Thermomechanical Coupling

INTRODUCTION

Adiabatic Shear Band (ASB) is a well known material alteration which takes place at very high speeds with materials having poor thermal conductivity. It results from the competition between plastic hardening and strain softening. Its formation can be divided into three stages as depicted in Figure 1-a. The first one is similar to standard stress-strain curve of a compression test where hardening behaviour is predominant to softening. In the second stage, both phenomena become equivalent, the ASB begins to occur. Through the latest stage, a very important drop of stress (about 80% of the maximum value) takes place. It is followed by a huge rise of temperature (about 500-700°C in Figure 1-b) leading to the creation of a very thin band (about few microns wide) of high temperature and large deformation: the ASB.

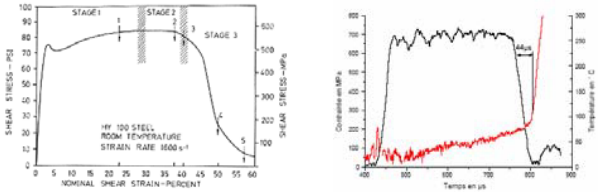

(a) (b)

FIGURE 1. (a) Stress-strain curve of a compression test at high speed issued from [2]. (b) Stress-temperature curve with respect to time for a compression test [3].

Although many researches have been conducted on the ASB phenomenon itself, only a few of them have been performed on ASB occurring in machining [1, 4, 5]. In [4], Owen and *al*. considered the ASB as a pure damage problem. The mesh refinement is guided by an isotropic error estimator which captures the progression of plastic deformation. The region of possible material failure is detected by evaluating an

CP908, *NUMIFORM '07, Materials Processing and Design: Modeling, Simulation and Applications*
edited by J. M. A. César de Sá and A. D. Santos

error indicator defined from a fracture criterion which is derived from the uncoupled integration of Lemaître's damage model. The authors have succeeded to simulate the first ASB for a 2D high speed orthogonal cutting test but, the used damage model shows mesh dependency. To avoid introducing damage, ASB can be considered as a pure deformation process [1, 5]. In [1], Bäker and *al.* have succeeded to simulate several ASB in this way, leading to the formation of a segmented chip using specific numerical techniques and adapted geometric criteria for the mesh refinement. In [5], Ortiz and *al.* used the calculation of an isotropic error, obtained from the Hessian computation, to automatically pilot the mesh adaptation. The control of mesh quality results from a coercive criterion on mesh size gradients. With purely adiabatic calculations, a localized shear band is detected and modeled for a cylinder implosion test including a small defect to onset the band formation. As the temperature increase and consequently the yield stress drop is rather small, the simulated phenomenon cannot exactly be considered as an Adiabatic Shear Band.

The aim of this paper is to use a fully automatic and process independent simulation procedure that allows detecting and following the formation of Adiabatic Shear Bands in 3D High Speed Machining.

NUMERICAL MODEL

Thermo-Mechanical Equations

The weak form of the momentum and incompressibility equations result into a mixed velocity-pressure formulation that is discretized by an enhanced (P1+/P1) quasi-linear interpolation based on a 4-noded tetrahedron element. Mechanical equations are implicitly solved by using Newton-Raphson algorithm, state variables are updated at each time increment by an explicit Euler scheme. The heat equation is solved by using the standard Galerkin formulation with a linear interpolation. The temperature time discretization uses a two time step scheme which is detailed in [6].

Isotropic Error Estimation and mesh adaptation

The goal of mesh adaptation triggered by error estimator is to confer to simulations an automatic fashion. In case of ASB, the adaptive strategy must be capable of detecting phenomena and automatically refining the mesh accordingly.

Definition of the Interpolation Error

For incompressible flows, the error related to the spherical part of the stress tensor is neglected. In the used [8] Zienkiewicz-Zhu approach, the exact error is estimated by approximating the exact solution s by a recovered superconvergent solution $\tilde{s}_h$ that is computed from the finite element one s_h. The estimation is then written in the energy norm:

$$\theta^{Z^2} = \left\| \tilde{e}_h \right\|_E = \left(\int_\Omega \eta(s_h) \left(\tilde{s}_h - s_h \right) : \left(\tilde{s}_h - s_h \right) d\omega \right)^{1/2} \quad (1)$$

Where $\left(s_h, \dot{\varepsilon}_h \right)$ are discretized deviatoric stress and strain rate tensors and $\eta(s_h)$ is the material viscosity.

Size maps for adaptive remeshing strategies

The optimality condition of the new mesh requires that the error is uniformly distributed among the new elements. The standard adaptive remeshing strategy, AST1, determines an optimized mesh T^{opt} that should satisfy a prescribed global accuracy θ^{imp}.

$$\theta^{imp} = \left(\sum_e^{Nbelt} \left(\theta_e^{opt} \right)^2 \right)^{1/2} \quad (2)$$

Where θ_e^{opt} is the contribution of element e on the optimal mesh to the global estimated error, and h_e is the size of element e.

In 3D, the number of elements of the optimal mesh is given by:

$$Nbelt^{opt} = \sum_e^{Nbelt} \left(\frac{h_e^{opt}}{h_e} \right)^{-3} \quad (3)$$

The optimal size of the element is finally computed by using the following equation:

$$h_e^{opt} = \left(\frac{\theta^{imp}}{\theta_e} \right)^{\frac{2}{2p+3}} h_e \quad (4)$$

Where p is the interpolation degree which is taken equal to 1.

For some problems, the computational cost resulting from mesh adaptation becomes higher and higher, so there is a risk to exceed computer capabilities. Consequently, a second approach, AST2, consists in determinating an optimized mesh T^{opt} for a prescribed number of elements $Neblt^{imp}$ providing the best possible accuracy. The optimal element size is still given by (4) but with the value of the global accuracy θ^{imp} as follows:

$$\theta^{imp} = \left(Nbelt^{imp}\right)^{-\frac{p}{3}} \left(\sum_{e}^{Nbelt} \left(\theta_e\right)^{\frac{6}{2p+3}} \right)^{\frac{2p+3}{6}} \qquad (5)$$

The error being uniformly distributed on the new elements, it is given by:

$$\theta^{uni} = \left(\theta^{imp}\right)^{\frac{2p+3}{2p}} \left(\sum_{e}^{Nbelt} \left(\theta_e\right)^{\frac{6}{2p+3}} \right)^{\frac{2p+3}{4p}} \qquad (6)$$

ALE Method: The Splitting Formulation

As ASB is a much localized phenomenon, the adaptive procedure provides highly refined meshes with strong gradients of the elements size, leading to unsatisfactory meshes. To avoid this and extreme mesh distortions due to machining conditions, an ALE method is employed. At each time step, it solves the thermal and mechanical equations using a pure Lagrangian formulation. This constitutes the first step of the implemented ALE splitting method [8].

Mesh Velocity Calculation

The second step of the ALE splitting method consists in computing the mesh velocity *w*, which can be different from the material one. *w* must satisfy the volume conservation condition on the boundaries:

$$(w - v).n = 0 \qquad (7)$$

Where *v* is the material velocity and *n* is either a consistent normal to the work piece on the free surface or the outside contact normal.

w is computed to optimize the elements quality, independently from the material deformation. The relationship between the material grid time derivatives of any variable φ is given by:

$$\frac{d_g \varphi}{dt} = \frac{\partial_m \varphi}{\partial t} + (w - v)\nabla\varphi \qquad (8)$$

The mesh velocity w_n of any node *n* is calculated by an iterative algorithm that computes the new location of nodes using a centring algorithm:

$$x_n^{it} = \frac{1}{|\Gamma_n|} \sum_{e \in \Gamma_n} x_{ge}^{it-1} C_e^{it-1} \qquad (9)$$

And then:

$$w_n^{it} = \frac{\left(x_n^0 - x_n^{it}\right)}{\Delta t} \qquad (10)$$

Where Γ_n is the set of elements contiguous to node *n* (i.e. which contain *n*), x_{ge} is the barycentre of element *e*, C_e^{it-1} is a weight factor insuring the mesh quality (see eq. (11) and (12)).

In order to optimize the mesh so that is obeys the optimal mesh size map h_e^{opt}, the weight factors of eq. (9) are turned into a combination of an adaptive coefficient Ca_e^{it-1} and a plain geometric coefficient Cf_e^{it-1} (which allows insuring the elements quality):

$$C_e^{it-1} = \left(1 - \zeta\left(Cf_{\min}^{it-1}\right)\right) \times Cf_e^{it-1} + \zeta\left(Cf_{\min}^{it-1}\right) \times Ca_e^{it-1} \qquad (11)$$

$$with \begin{cases} Ca_e^{it-1} = \left(\frac{h_e^{opt}}{h_e^{it-1}} \right)^3 \\ Cf_e^{it-1} = \chi \frac{\left[V_e^{it-1}\right]^+}{\left(p_e^{it-1}\right)^3} \end{cases} \qquad (12)$$

Where V_e is the volume of element e, p_e is its perimeter, and χ is an adimensional constant such that Cf is equal to 1 for a perfect tetraedra. ζ is a smoothed Heaviside function, such that $\zeta(C_f)$ is equal to 0 if Cf is larger than the critical value Cf_{crit} and else equal to 1 (with a smooth variation between 0 and 1).

Convective phase

A first order linearization of eq. (13) yields a quick and simple way to transport P1 nodal variables.

$$\varphi_{ALE}^{t+\Delta t} = \varphi_{LAG}^{t+\Delta t} - (v - w).\nabla\varphi^{t+\Delta t} \qquad (13)$$

As φ is linear, $\nabla\varphi$ is constant on each element, so the gradient $\nabla\varphi^{t+\Delta t}$ is computed in the upwind element. This method can not straightforwardly be applied to transport the P0 variables that are stored at integration points (the barycentres of the elements) because their finite element gradient is not known. Therefore, a Lagrangian like transport has been preferred. A recovered continuous solution is directly constructed on patches centred at integration points. For more details about the utilised ALE formulation, see [8].

THERMOMECHANICAL COUPLING

ASB is a highly-coupled thermo-mechanical phenomenon: the heat generated by deformation makes the yield stress decrease, leading to more heat creation. In the following, several thermo-mechanical coupling schemes are investigated, from less to more coupled ones.

Description of Coupling Formulations

Incremental Thermo-Mechanical Coupling

At each time step, the mechanical equations are first solved using thermal data computed at the previous time increment, and then the heat equation is solved with newly calculated mechanical values. This

scheme is very fast but requires using very small time step to model strong coupled problems.

Strong Thermo-Mechanical Coupling, by Using a Fixed Point Algorithm

The scheme is initialized by the incremental one, the iteration are carried out using the newly calculated temperature value, until variations are small between successive iterations. This scheme provides a strong coupling but, as a fixed point algorithm, its convergence is not ensured.

Strong Thermo-Mechanical Coupling, by Using the Newton-Raphson's Algorithm

With T corresponding to the temperature, the fully coupled thermo-mechanical problem *(v, p, T,)* is implicitly solved by using the Newton-Raphson algorithm. A single system is iteratively solved until convergence. This method strongly couples the thermo-mechanical equations. As a higher order algorithm, it is more robust and efficient but requires solving larger systems, so requiring more computational time (about $\left(\frac{4}{3}\right)^{3/2}$ in 3D).

Comparisons on a compression test

The three previous methods are compared on a 25% hot compression test performed at 1 m/s (Figure 2).

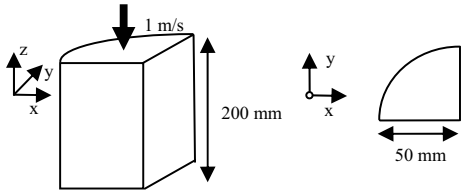

FIGURE 2. Hot Compression test performed on ¼ of a cylindrical sample at 1 m/s.

The sample consists of a Titanium alloy (Ti6AlV4). which is described by the following visco-plastic constitutive laws (14) (see table 1 for corresponding numerical values).

$$\bar{\sigma}\left(\bar{\dot{\varepsilon}}, T\right) = Ke^{-\beta T}\left(\bar{\dot{\varepsilon}}\right)^{m-1} \qquad (14)$$

Where m the strain rate sensibility coefficient and $\bar{\dot{\varepsilon}}$ the equivalent strain rate.

TABLE 1. Numerical Values of Parameters Used in the Previous Visco-plastic Constitutive Law.

Parameter	Numerical Value
K	43,872 MPa
β	0.00564 K^{-1}
m	0.152

The used mesh is made of 2,800 nodes and 13,500 elements.

Weak Physical Coupling

In figure 3, it can be observed that all schemes give exactly the same results in terms of temperature and strain rate, which allows validating the algorithms. As expected, the incremental coupling method is the fastest one (338 s) whereas the fully coupling scheme is the longest (2,139 s). It shows that incremental coupling is both accurate and fast in case of non intense physical coupling.

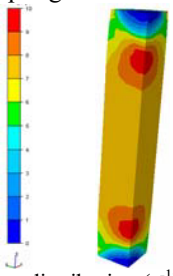

FIGURE 3. Strain rate distribution (s^{-1}) for the Incremental, Fixed Point and Fully Implicit (c) schemes.

Strong Physical Coupling

In order to test stronger physical coupling, the value of β has been decreased to 0.00282 K^{-1}. It turns out that the incremental algorithm does not provide the same results as the other schemes (Fig. 4). This confirms that the incremental coupling scheme is inaccurate when the physical thermo-mechanical one is intense.

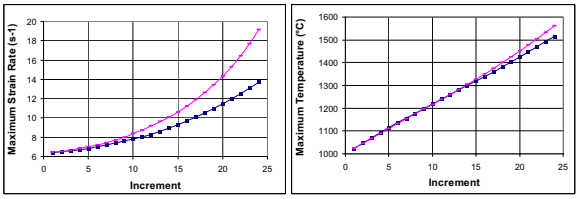

(a) (b)

FIGURE 4. Maximum strain rate (a) and temperature (b) for the weak (blue-square) and strong (red-line) coupled schemes as a function of time.

Very Strong Physical Coupling

The physical coupling is further increased by dividing by 3 the initial value of β (0.00188). It turns out that, not only the incremental method provides

very different results (Fig. 5) but also the fixed point method does not converge at any time steps contrarily to the fully implicit one. It shows that, in case of intense physical coupling, the implicit is a mandatory.

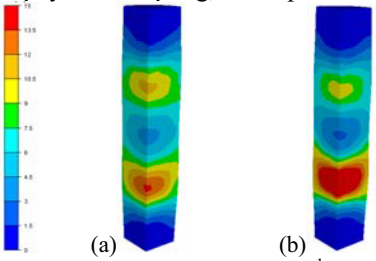

(a) (b)

FIGURE 5. Strain rate distribution (s^{-1}) for the Incremental (a) an Fully Implicit (b) schemes

APPLICATION TO MACHINING

Physical Model

The constitutive equation for the Ti6AlV4 presented in more details in [1, 6] is written as:

$$\begin{cases} \bar{\sigma}\left(\bar{\varepsilon},\dot{\bar{\varepsilon}},T\right) = K^{*}\Psi(T)\bar{\varepsilon}^{n^{*}\Psi(T)}\left(1+C\ln\left(\frac{\dot{\bar{\varepsilon}}}{\dot{\bar{\varepsilon}}_{0}}\right)\right) \\ \Psi(T) = \exp\left(-\left(\frac{T}{T_{MT}}\right)^{\mu}\right) \end{cases} \quad (15)$$

Where $\bar{\sigma}$ and $\bar{\varepsilon}$ respectively are the equivalent stress and deformation. $K^{*}, n^{*}, T_{MT}, \mu$ and C are constant values that are given in [9].

Because of extreme temperature rise in ASB, material parameters like conductivity and heat capacity are regarded as temperature dependant. A linear interpolation between points at 24°C and 1200°C, which details can be found in [6], is used.

Finally, it is assumed that there is no heat transfer between the deformed material and the cutting tool, which is also considered as perfectly rigid. Friction on the cutting edge is regarded as negligible as such speeds [1].

Orthogonal cutting

In order to evaluate the numerical model, results have first been compared to Bäker's [1] for a high speed orthogonal cutting configuration described in Figure 6 (Dimensions are summarized in table 2).

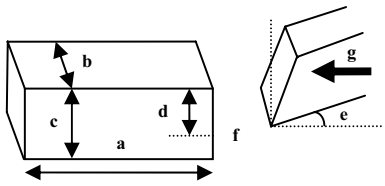

FIGURE 6. High speed orthogonal cutting configuration

TABLE 2. Orthogonal Cutting Test Values Described in Figure 6.

Value description	Numerical value
Length (a)	0.28 mm
Width (b)	0.04 mm
Height (c)	0.15 mm
Cutting depth (d)	0.04 mm
Cutting angle (e)	10°
Roundness of the tool (f)	3 mm
Cutting speed (g)	50 m/s

In order to model plane strains, symmetry planes have been added on both lateral faces of the 3D mesh, which has a maximum of 29,000 nodes and 140,000 elements.

Comparison with Baker's Results

Figure 7 shows that both models give same results in terms of strain distribution, which has also been confirmed by analyzing the cutting force evolution in [6]. The difference between chip curvatures is explained by the different tool edge radii used in both models, the one utilized here being more realistic. From those results, obtained after four days on a P IV, 3.20 GHz with 2Go of RAM, it can be concluded that the developed model is capable of simulating ASB in 3D orthogonal cutting without any preliminarily information (Figure 8) for the numerical model.

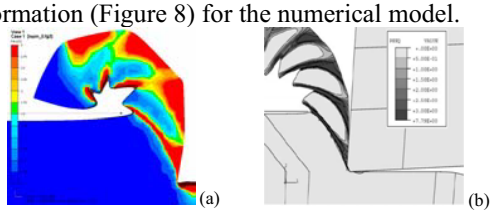

(a) (b)

FIGURE 7. Strain distribution for present (a) and Bäker (b) models. The scale has been cut to 3.0.

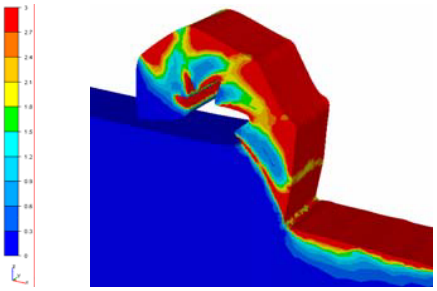

FIGURE 8. Strain distribution in a 3D segmented chip obtained by high speed orthogonal cutting (50 m/s)

Numerical Investigation

Figure 9 shows that mesh refinement automatically occurs where Von Mises stress drops, allowing the detection of ASB formation.

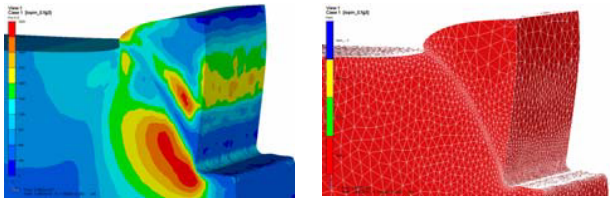

FIGURE 9. Von Mises stress distribution and corresponding mesh at the establishment of the first ASB.

In order to evaluate the accuracy and reliability of the results, it is required to check the mesh dependency. Table 3 presents the bandwidth obtained for several model sizes. It shows a relative difference of about 3.4 % when multiplying by 2 the number of elements in the ASB, which indicates that the computed ASB width converges to a finite value which does not depend on the mesh size.

TABLE 3. Band Width for Different Model Sizes.

Elements number of the models	Elements number in ASB	Band width (µm)
54,000 (a)	4-5	3.49
130,000 (c)	8	3.40
260,000 (d)	10	3.38

Blanking

A 3D blanking test is considered in order to study more actual 3D simulation of ASB. Problem dimensions (Fig. 10) are taken close to the previous orthogonal cutting values with the same material (see Table 4).

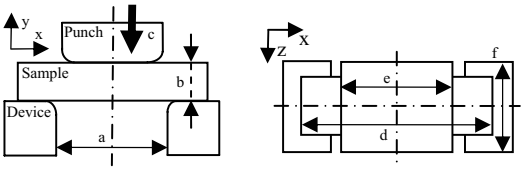

FIGURE 10. High speed blanking test configuration

TABLE 4. 3D Blanking Test Conditions Described in Figure 10.

Value description	Numerical value
(a)	0.093 mm
(b)	0.045 mm
Cutting speed (c)	50 m/s
(d)	0.3 mm
(e)	0.085 mm
(f)	0.08 mm
Edge radii	0.003 mm

Number of nodes and elements of the corresponding mesh are respectively limited to 29,000 and 140,000.

Application to Blanking

In Figure 11, the Von Mises drop band captured by mesh adaptation is observed. Consequently, a high temperature band appears. These results, obtained after 24 hours of calculations, indicate the ASB formation. It confirms the capability of the code to simulate ASB in various 3D cutting configurations. It has been noticed that such ASB formation is not observed under more conventional (size, speed, material) configurations.

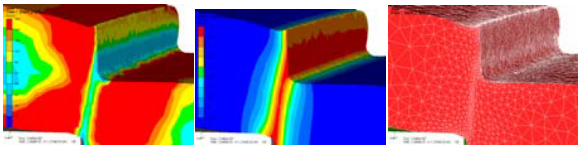

FIGURE 11. Von Mises, temperature and mesh distributions for the high speed blanking test

REFERENCES

1. M. Bäker, J. Rösler, C. Siemers, "A finite model of high speed metal cutting with adiabatic shearing", *Comp. and Struct.*, 80 (2002), pp. 495-513.
2. T.W. Wright, G.K. Batchelor, L.B. Freud, "The Physics and Mathematics of Adiabatic Shear Bands", *Cambridge University Press*, 2002.
3. N. Ranc, "Etude des Champs de Température et de déformation dans les matériaux métalliques sollicités à grande vitesse de déformation", PhD Thesis, University of Paris X – Nanterre
4. D.R.J. Owen, M. Vaz Jr., "Computational techniques applied to high speed machining under strain localization conditions", *Comp. Meth. in App. Mech. and Eng.*, 171 (1999) , pp 445-461.
5. J.F. Molinari, M. Ortiz, "Three-dimensional adaptive meshing by subdivision and edge-collapse in finite-deformation dynamic-plasticity problems with application to adiabatic shear banding", *Int. J. for Num. Meth. in Eng.*, 53 (2001), pp 1101-1126.
6. F. Delalondre, S. Guerdoux, L. Fourment, "3D simulation of high speed orthogonal metal cutting with adiabatic shearing", submitted to *Comp. and Struct.*.
7. R. Boussetta, T. Coupez, L. Fourment, "Adaptive remeshing based on a posteriori error estimation for forging simulation", *Comp. Meth. in Appl. Mech. and Eng.*, Vol. 195, pp. 48-49.
8. L. Foument, S. Guerdoux, "Enhanced transport and remeshing schemes for ALE formulation applied to Friction Stir Welding", Proc. of the 9th *Esaform Conf. on Mat. Form.*, UK, April 26-28, 2006
9. M. Bäker, "The Influence of Plastic Properties on Chip Formation", *Comp. Mat. Sc.*, 28 (2003), pp 556-562.